ORIGINAL ARTICLE

Fatigue & Fracture of Engineering Materials & Structures

Edge tracing technique to study post–necking behavior and failure in Al–alloys and anisotropic plasticity in line pipe steels

Zacharie Shokeir[1,2*] | Jacques Besson[2] | Chiraz Belhadj[2,3] | Tom Petit[1] | Yazid Madi[2]

[1]Université Paris-Saclay, CEA, DES - Service d'Etude des Matériaux Irradiés, 91191, Gif-sur-Yvette, France

[2]MINES Paris, PSL Research University, Centre des Matériaux, CNRS UMR 7633, BP 87, 91003, Evry, France

[3]GRTgaz Research & Innovation Centre for Energy (RICE), Villeneuve-la-Garenne, 92390, France

Correspondence
Zacharie Shokeir, Université Paris-Saclay, CEA, DES - Service d'Etude des Matériaux Irradiés, 91191, Gif-sur-Yvette, France
Email: zacharie.shokeir@mines-paristech.fr

Funding information
Université Paris-Saclay, CEA; GRTgaz, RICE

The recently developed Edge Tracing (ET) method allows to estimate the radial deformation in axisymmetric tensile specimens via analysis of digital images recorded during the experiments. Images are processed to detect the sample's contours and therefore, estimate the minimal cross–section diameter. This technique was mainly developed to characterize the elastic–plastic behavior well beyond the necking strain. The aim of this work is to extend the ET method to two case studies. Firstly, the post–necking behavior and failure of a low ductility Al–alloy are investigated. Low ductility alloys tend to fail brutally after reaching the maximum load. The major result is the capture of the sharp load drop which allowed to calibrate parameters of a GTN damage model. Secondly, the anisotropic elastic–plastic behavior of a "vintage" line pipe steel is characterized by a direct measurement of the Lankford coefficient. Assembled experimental data allowed to model the anisotropic plasticity in different loading directions.

KEYWORDS
Edge tracing technique, Aluminum alloys, Failure assessment, GTN model, Line pipe steels, Plastic anisotropy, Large strains

Abbreviations: ET, Edge Tracing; AA, aluminum alloy; ST, simple tension sample; NT, notched tension sample; GTN, Gurson-Tvergaard-Needleman model.

1 | INTRODUCTION

Engineering problems modeled by the finite element method require in some cases sufficient information about the large deformations occurring in the material. Metal forming and ductile failure are perfect examples of cases that necessitate the material's response prior and beyond the necking strain [1;2]. Tensile tests carried out on round dog bone simple tensile samples (ST) provide the material's engineering stress—strain curve. During testing, diffuse necking occurs as the plastic deformation is localized in a thin ligament called the "neck". At this phase, the stress triaxiality increases in the neck. The output stress—strain curve must then be corrected to obtain a full true stress—logarithmic strain curve. The most commonly used correction equation is proposed by Bridgman [3] and is modified by Bao *et. al.* [4]. Other authors as Tu *et. al.* [2;5], Versaillot *et. al.* [6], Bao *et. al.* [7], Bai *et. al.* [8] and Mirone [9] point out the fact that the Bridgman correction leads to significant errors. Therefore, they develop other analytical corrections to obtain the true stress—logarithmic strain curve.

Zhang *et. al.* [10] propose to use round notched tensile bars (NT) as an alternative method for the assessment of the material's behavior at large strain. Diameter reduction can be recorded by a radial extensometer located at the specimen's minimum cross section. The difficulty of this setup is to assure that the extensometer does not slide so that the measurements are continuously taken at the minimum cross section. Moreover, the extensometer knife-edges may damage the notch surface and affect the test results [11]. The cited authors apply the above explained experimental procedure using radial extensometers to obtain load—diameter reduction curves in welded joints in a high strength 690 MPa structural steel. The true stress—strain curves are then obtained using a correction factor on the net stress. The correction factor is a function of the notch geometry and the maximum recorded load.

Later, Hopperstad *et. al.* [12], Vilamosa [13] *et. al.* and Tu *et. al.* [2;14] proposed the Edge Tracing (ET) method to obtain the diameter reduction of ST and axisymmetric NT specimens via analysis of digital images taken during the experiment. Digital high-speed camera(s) are used to take pictures which are each associated to the corresponding load. Each image is analyzed separately by simple algorithms to correlate the given load to a radial deformation calculated by detecting the smallest cross-section diameter in the notch. Each pixel in the $8bits$ image represents a gray value ranging from 0 to 255. The specimen contour can be detected only if a sharp contrast is maintained between the specimen and the background. Accordingly, the section reduction is calculated at the output. More details concerning the method are given in the following section. The ET method is applied in the work of Hopperstad *et. al.* [12] to study the effect of strain rate and stress triaxiality on the plastic flow of Weldox 460 E steels. Tu *et. al.* [2;14] use the ET method to study the effect of low temperature ($-60°C$) on the total deformation at failure of a 420 MPa structural steel. Mirone *et. al.* [15] use a simplified ET method to investigate the effect of strain rate and temperature on the necking onset and hardening of a A2-70 stainless steel.

The ET method is therefore a suitable candidate for acquiring knowledge about the material behavior at large deformations via the stress—radial deformation curve. The latter holds significant amounts of information regarding the large pre– and post–necking deformations. The aim of this work is to extend the utilization of the ET method to study two challenging mechanical problems not mentioned above:

1. The post–necking behavior of low ductility aluminum alloys is investigated. Aluminum alloys with a high content of secondary phases in the metallic matrix are susceptible to void nucleation on these phases under mechanical loading [16]. The created voids increase in size and coalesce rapidly leading to premature failure. The post–necking behavior of these alloys is extremely hard to analyze since the material tends to fail brutally after reaching its maximum bearing load. However, a combination of deformation controlled testing together with the ET method can help obtain enough information in the post–necking phase of these alloys. This method is presented in the current study. Afterwards, a damage model can be fit by making use of the post–necking phase of the tensile tests.

2. The anisotropic plastic behavior of a vintage line pipe steel is studied. Steels can undergo a hot/cold rolling process to obtain the desired shape and dimensions. During the rolling process, a specific crystallographic texture can emerge which leads to an anisotropic plastic behavior. In order to study the tensile behavior of these steels, samples are fabricated along different directions with respect to rolling direction. The ET method can be applied to these tests in order to study the radial deformation in the two orthogonal directions during the test. Based on the experimental results, a model for anisotropic plasticity can be obtained.

In the following section, the testing apparatus is described as well as the image analysis process. In the third section of this paper, a case study on failure assessment in a 6061-T6 aluminum alloy is carried on NT specimens using the ET method. NT specimens can cover a wide range of stress triaxiality levels (0.6–2.0) that can be used to calibrate damage models. The chosen alloy has a challenging feature: its brief necking phase (*i.e.* failure occurs brutally after reaching the maximum force). In the fourth section of this paper, a case study is carried on a X52–API grade steel to highlight the ET method's advantages in determining the anisotropic plastic behavior of textured materials. Parameters of a plastic flow law with an anisotropic criterion are determined by the analysis of the tensile tests prior the onset of failure.

2 | SPECIMENS AND EXPERIMENTAL TECHNIQUES

2.1 | Specimens and testing

In this study, tests are carried on smooth (ST) and notched (NT) axisymmetric tensile specimens. Fig. 1 shows a sketch of the NT specimens. For a fixed minimum cross-section diameter (Φ_0), varying the notch curvature radius R_0 results in different stress triaxiality levels[17]. Given the initial curvature radius R_0 and minumum cross-section diameter Φ_0, each NT sample gets its name as follows: NTX = 10 R_0 / Φ_0, where X is the sample's name (*e.g.* NT10, NT4, NT2). Small 'v' notches are also machined in the specimens beyond the notch area to easily attach an axial extensometer (gauge length L_0 in fig. 1) during the test. The 'v' notches prevent the extensometer knives from sliding. Smooth tensile bars are machined following the ASTM–E8 standard. The exact dimensions (R_0, Φ_0, L_0) are detailed in each case study.

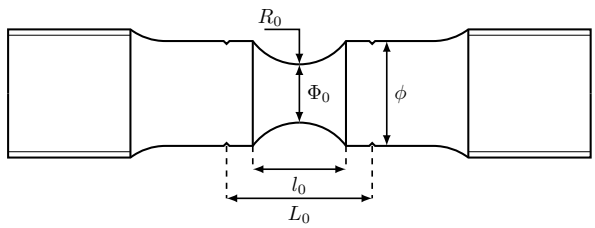

FIGURE 1 Geometry of NT tested samples. $\phi = 1.8 \times \Phi_0$. Each NT sample gets its name as follows: NTX = 10 R_0 / Φ_0, where X is the sample's name (*e.g.* NT10, NT4, NT2).

Figure 2 shows the test setup for ST and NT specimens. The knife–edged extensometer is attached to the sample by rubber

bands and is used to control the machine displacement as well as to measure the axial displacement. All experiments are carried at room temperature. Tests are carried out using a strain rate of about $5.\,10^{-4}$ s^{-1}. The gauge length used to calculate the strain rate in NT samples corresponds to the notch length in the axial direction (l_0 in fig. 1). The strain rate in notched specimens is then approximated to the ratio between the machine displacement rate and l_0.

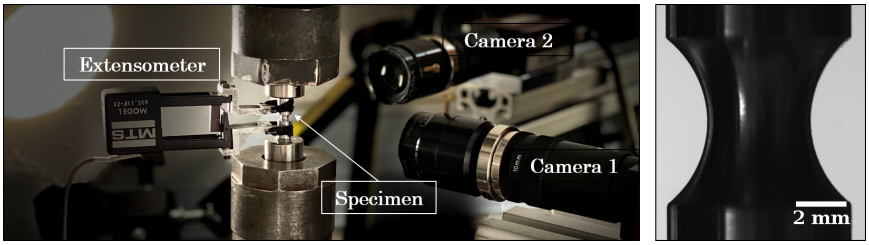

FIGURE 2 Test setup of deformation controlled ST and NT experiments. Two digital cameras on two orthogonal planes with retro-lighting are required to obtain a significant difference between the sample and the background gray levels as shown. The knife–edged extensometer is attached to the sample by rubber bands and used to control the machine displacement as well as to measure the axial displacement.

Time, load, machine displacement and extensometer opening are continuously monitored during the test. The digital cameras are placed on two orthogonal planes to record images taken against a white background retro–lit by two LED lamps (see fig. 2). The cameras are fixed in the directions of interest. The testing machine controller is used to trigger image capturing (1 image/second). The setup is designed in order to obtain a high contrast between the specimen and the background to facilitate image processing.

Tests conducted using a machine displacement control may display an unstable behavior after the onset of the sharp load drop which corresponds to crack initiation. To be able to record the post–crack initiation behavior, tests are conducted using an extensometer opening control (hereby referred to as "deformation control"). The results are exemplified in fig. 3 which displays both force—machine displacement and force—extensometer opening curves. The slope of the curve after the crack initiation is steeper in the first case which explains why machine displacement control leads to an instability as explained in [18].

2.2 | The Edge Tracing (ET) method

Two digital cameras with a resolution of 2048×2048 pixels are placed on two orthogonal planes as shown in fig. 2 and used to acquire high resolution images. Images are saved as 8bit grayscale (grayscale levels range from 0 (black) to 255 (white)). The retro–lighting should be correctly adjusted to obtain a significant difference between the sample and the background gray levels. The images are then treated using a PYTHON script which detects the specimen contours, evaluate the minimum diameter ($\phi_{\min}$) and the notch curvature radius (R). The main steps of the algorithm used to process the images are explained below:

1. The input image is filtered by a non-local image denoising method [19] in order to enhance the sharp gray level contrast between the sample and the background, see fig. 4 (a).
2. The image is manipulated as an array of pixels. For each j^{th} row of pixels in the array:
   a. A threshold is defined (via the OTSU method [20]) to detect the sample's contour. This threshold is used to define the sample's contour and thus, the diameter ("Pixel raw distance" in fig. 4 (b)).
   b. The "Raw signal" in fig. 4 (b) is then interpolated to get an accurate estimation of the gray transition interface (sample–white background interface) at the sub–pixel level ("Pixel interpolated signal" in fig. 4 (b)). The diameter on the j^{th} row

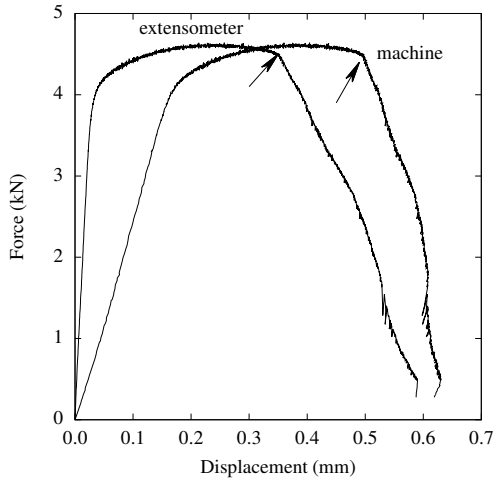

FIGURE 3 Test control for a test conducted on a NT10 (6061-T6 Al alloy). Load vs. machine displacement and Load vs. extensometer opening. Arrows point to the failure initiation.

of the image array is estimated via the "Pixel interpolated distance" in fig. 4 (b).

c. Steps **a** and **b** are repeated on all rows in the array to trace the whole sample's contour and then deduce the minimum cross–section diameter Φ_{min}, see fig. 4 (c).

3. Once the sample's contour is traced, the notch curvature radius R can be estimated. The arc used to fit the notch radius on the left and right contours is restricted between two limits located at $\pm\,\eta\,\Phi_{min}$ (see green arcs in fig. 5 (a)). The effect of η on the calculated R is illustrated in fig. 5 (b). The latter shows the estimated R as a function of η for a given level of plastic deformation. The best range of η lies between 0.5 and 1.0. For each sample, an optimal value of η must be given to the algorithm for the computation of R. As shown in fig. 4 (b), η does not affect the computed R at low deformation levels (*e.g.* $\Delta\Phi/\Phi_0 = 2.6\%$) as the notch curvature radius can be fit by a circle. However, η has a significant effect on the computed R at high deformation levels (*e.g.* $\Delta\Phi/\Phi_0 = 13.57\%$ shown in fig. 4 (b)) since re-notching might occur and thus, the sample's notch cannot be fit by a circle anymore. One can note that the Bridgman correction (and similar corrections based on the notch curvature radius) cannot be applied to such high deformation levels with the renotching effect.

During testing, a series of images is taken (1 image/second) and then analyzed by the ET method to calculate $\frac{\Delta\Phi}{\Phi_0}$ and the notch curvature radius R. The Φ_{min} of the first image corresponds to a number of pixels that is used as a reference Φ_0 for calculating the radial deformation: $\frac{\Delta\Phi}{\Phi_0}$. The images may be cropped to reduce the computation time by only taking into account the zone of interest around the notch.

After testing and only if the test is interrupted before complete fracture, the sample's notch is laser scanned to measure the notch diameter every 0.1 mm in the longitudinal axis. The notch is then virtually reconstructed by the stack of measurements to calculate the Φ_{min} and compare to the ET measurement (see 3.2).

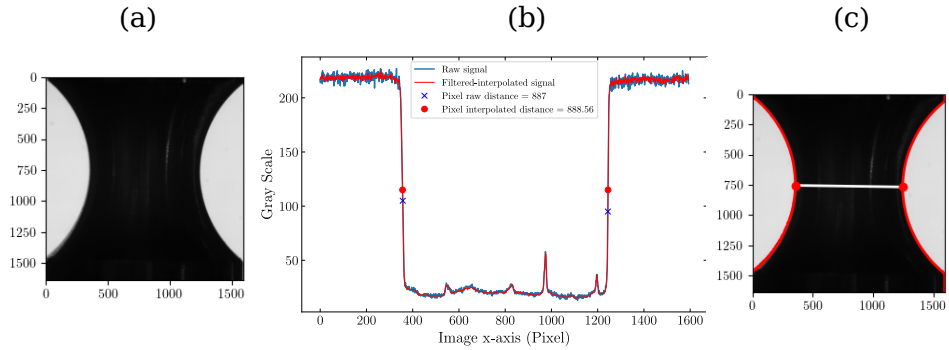

FIGURE 4 (a) Filtered input image to enhance the sharp gray level contrast between the sample and the background. (b) Contour tracing and diameter detection for each row in the image pixel array. (c) Minimum cross–section diameter Φ_{min} detection after treating all rows in the image array. The step-by-step ET method is explained in the text.

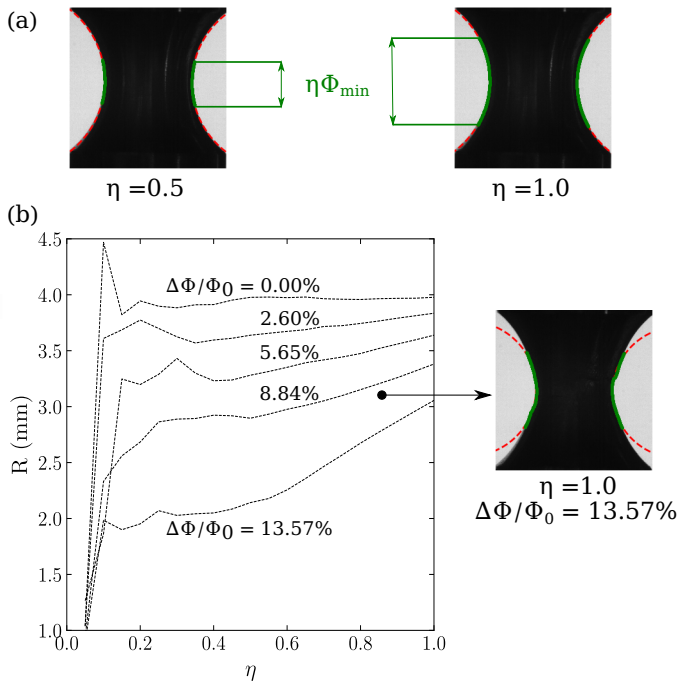

FIGURE 5 (a) Illustration of η and its effect on the limited area shaded by green arcs and used for estimating the notch curvature radius R. Two values of η are given and their limited area corresponds to $\pm\eta\,\Phi_{min}$ where Φ_{min} is the minimum cross section diameter. (b) Calculated notch curvature radius R as a function of η. At high deformation levels, the notch cannot be fit by a circle.

3 | CASE STUDY 1: PLASTICITY AND FAILURE OF A 6061-T6 ALUMINUM ALLOY

3.1 | 6061-T6 aluminum alloy

The studied 6061-T6 aluminum alloy has two major alloying elements (Mg and Si) as shown in tab. 1. Both elements form nano–sized Mg_xSi_y precipitates during the 8 hours age hardening treatment at 175°C (T6 heat treatment[21]). The alloy is characterized by a 255 MPa yield strength, 305 MPa tensile strength, and a 7.5% uniform elongation. Coarse Mg_2Si spherical precipitates ($\sim 5\mu$m) as well as iron rich particles ($\sim 10\mu$m long) are also present in the matrix; they are considered as damage initiators during straining[22;23].

TABLE 1 Studied AA6061-T6 chemical composition by %wt.

Mg	Si	Fe	Cu	Cr	Mn	Zn	Ti	Al
0.58	1.00	0.16	0.28	0.19	0.06	0.03	0.02	bal.

3.2 | Tests on NT and ST tensile specimens

The studied specimens have a minimal diameter Φ_0 of 4 mm and a radius R_0 equal to 4, 1.6 and 0.8 mm (respectively corresponding to NT10, NT4 and NT2 specimens). The extensometer initial length (L_0) is 10 mm for NT specimens and 17.8 mm for ST specimens. Tests are carried by the deformation control technique to capture the post–necking phase. Recorded images are treated to obtain the radial deformation. Fig. 6 shows the macroscopic mechanical behavior of ST, NT10, NT4, and NT2 samples (two samples are tested from each geometry). The sharp load drop observed on all specimens corresponds to a crack initiation at the center of the specimens. The crack propagates towards the free surface up to full failure. These tests are usually unstable and the load decrease cannot be controlled unless the deformation control technique described above is applied. The controlled load drop is more difficult to achieve for NT2 and ST specimens.

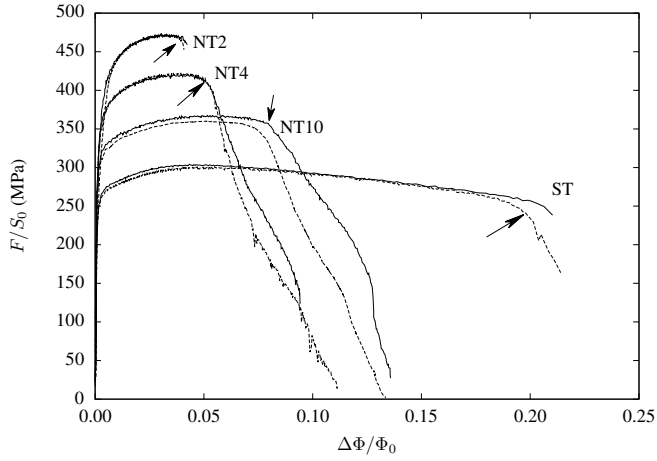

FIGURE 6 Deformation controlled ST and NT tensile tests (AA6061-T6). Two tests are shown (solid and dashed lines) for each specimen type. Arrows indicate fracture initiation.

Some specimens are interrupted before complete failure. The specimens are then laser scanned to map their diameters as a function of the axial position (every 0.1 mm) and the viewing angle (every 5°). Results can then be compared to the ET measurements. This comparison is shown in fig. 7 for the minimum cross–section diameter in a NT10 specimen. The ET measurement compared to the scan shows good agreement with a maximum absolute difference of 0.014 mm between both measurements. The measured difference is attributed to the specimen surface roughness due to the deformation of large grains (mean grain size 30 μm). Therefore, the radial deformation calculated by the ET method gives an accurate estimate of the real radial deformation that would have been measured by radial extensometers.

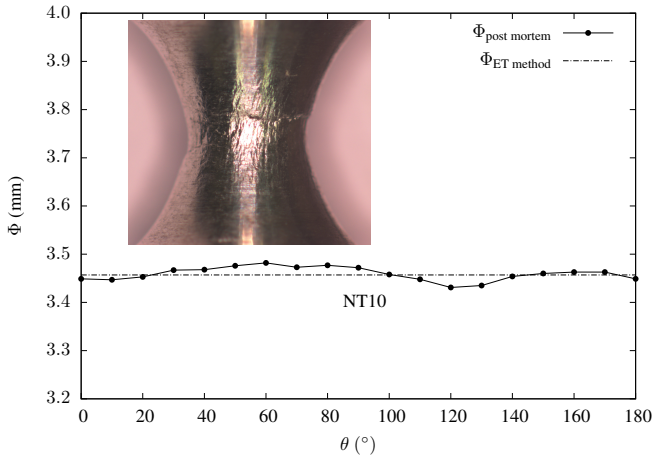

FIGURE 7 Minimum cross–section notch diameter Φ_{min} laser scanned after an interrupted NT10 test compared to the final Φ_{min} obtained by the ET-method. Image showing the initiated crack on the surface of the interrupted NT10 test.

3.3 | Using the ET measurements to model the material behavior: plasticity

With the increasing efficiency of computers, it is now possible to use optimization methods based on finite element simulations of specimens to adjust the elastic–plastic behavior on the experimental results. The method uses the difference between experimental and finite element results as an objective function to be minimized. This "brute force" methodology is recently employed in [24;25]. The fit of the hardening function is first done assuming von Mises plasticity; this assumption is validated after fitting. The fit is performed using the load—diameter reduction curves before the onset of sharp load drop (see arrows in Fig. 6). Elongation up to the onset of necking and diameter reductions for all specimens are used to define the objective function. The flow stress σ_F is expressed as a function of the accumulated plastic strain p as:

$$\sigma_F(p) = \sigma_0 + Q_1(1 - \exp(-b_1 p)) + Q_2(1 - \exp(-b_2 p)) \tag{1}$$

where σ_0, Q_1, b_1, Q_2 and b_2 are coefficients to be fit. The fitting is done by minimizing the value of the objective function mentioned above. The optimized values are: $\sigma_0 = 243$ MPa, $Q_1 = 85$ MPa, $b_1 = 17.4$, $Q_2 = 17.5$ MPa and $b_2 = 262$.

In the following section, use is made of the sharp load drop part of the curve corresponding to crack propagation in the minimum cross section (beyond arrows in Fig. 6) to fit parameters of a damage model.

3.4 | Using the ET measurements to model the material behavior: Ductile damage

The ductile failure of an AA6061-T6 is characterized by a void nucleation phase on intermetallic particles, followed by growth of these microcavities and their coalescence [26;22;23;27]. The AA6061-T6 along with other ductile alloys containing micron sized precipitates undergo a void nucleation phase during loading. This phenomenon is not easy to model since the damage must be studied on various stress triaxiality levels to fit a well predictive damage model. The failure of the AA6061-T6 is often simulated by the GTN model [28;29;30] to take into account the void nucleation, growth and coalescence. Parameters of this model can be determined by the aid of *insitu* experiments and/or unit cell simulations [22;31;32;33;34;35]. In both cases, all these authors agree that the porosity evolution in this model is sensitive to the stress triaxiality.

3.4.1 | Gurson damage model

The GTN model used in this work is fully described below. The model uses the void volume fraction (f) as a damage variable. The porosity is expressed as the sum of the porosity due to void growth (f_g) and the porosity due to void nucleation (f_n) [36]. The model is based on the definition of an effective stress ($\sigma_\star$) used to define the yield condition as follows [37]:

$$S = \sigma_\star - \sigma_F(p) \tag{2}$$

where σ_F is the flow stress of the undamaged material. The plastic strain rate tensor is obtained using the normality rule as follows:

$$\dot{\varepsilon}_p = (1-f)\dot{p}\frac{\partial S}{\partial \boldsymbol{\sigma}} \tag{3}$$

where $\boldsymbol{\sigma}$ is the Cauchy stress tensor. The plastic multiplier $\dot{p}$ is such that $\dot{\varepsilon}_p : \boldsymbol{\sigma} = (1-f)\dot{p}\sigma_\star$. $\dot{p}$ is obtained either using the consistency condition (rate independent case) or a visco–plastic flow rule (rate dependent case). In the specific case of the GTN model, the effective stress is implicitly defined as a function of the stress tensor and the porosity by the following equation:

$$\left(\frac{\sigma_{\text{eq}}}{\sigma_\star}\right)^2 + 2q_1 f_\star \cosh\left(\frac{3}{2}q_2\frac{\sigma_m}{\sigma_\star}\right) - 1 - {q_1}^2 f_\star^2 \equiv 0 \tag{4}$$

where σ_{eq} is the von Mises equivalent stress, and σ_m the mean stress. q_1 and q_2 are two model parameters describing void growth. $f_\star$ is defined such that:

$$f_\star = \begin{cases} f & \text{if } f < f_c \\ f_c + \delta(f - f_c) & \text{otherwise} \end{cases} \tag{5}$$

where the "acceleration" factor $\delta \geq 1$ is expressed as:

$$\delta = \frac{1/q_1 - f_c}{f_R - f_c} \tag{6}$$

The function $f_\star$ is used to represent void coalescence in a simple way. Coalescence is assumed to start when f reaches a critical value f_c. f_R represents the porosity at failure. Void growth is directly obtained from the plastic flow (mass conservation) as

$f_0{}^\dagger$	$q_1{}^\dagger$	$q_2{}^\dagger$	$f_c{}^\dagger$	$f_R{}^\dagger$	$p_c{}^\dagger$	$f_N{}^\dagger$	$\sigma_0{}^\dagger$	A_n^s	A_n^0	N	$h^\dagger$
0.0035	2.	1.	0.05	0.2	0.03	0.0215	250 MPa	0.11	0.02	4	0.1 mm

TABLE 2 Parameters of the GTN ductile damage model. Parameters marked with a † are *a priori* fixed while the remaining parameters are calibrated via the ET method.

follows:

$$\dot{f}_g = (1-f)\text{trace}\left(\dot{\boldsymbol{\varepsilon}}_p\right) \tag{7}$$

Void nucleation plays an important role in the failure process. Assuming strain controlled nucleation[28], the nucleation rate can be expressed as shown:

$$\dot{f}_n = A_n \dot{p} \tag{8}$$

where A_n is a function of the material state which is often expressed as a function of the plastic strain p[28;38] but may also depend on the stress state[39;23]. The following nucleation law (A_n) is adjusted by trial and error following the ideas proposed in[23]:

$$A_n = A_n^s \left\langle \sigma_{I\star}/\sigma_0 - 1 \right\rangle^N + A_n^0 \tag{9}$$

where σ_0, A_n^s, A_n^0 and N are parameters to be identified via experimental data. Eq. 9 accounts for the stress effect on nucleation in the first part ($A_n^s \langle ... \rangle$) and the plastic deformation in the second added part (A_n^0). The parameter σ_0 is a critical stress threshold below which the first nucleation term is not activated. The effective maximum principal stress ($\sigma_{I\star}$) is defined as the ratio between the effective stress and equivalent von Mises stress multiplied by the maximum principal stress (*i.e.* $\sigma_{I\star} = \sigma_I \times \frac{\sigma_*}{\sigma_{\text{vM}}}$). Nucleation is only active if:

1. The plastic strain p is larger than a critical strain p_c (taken from[23] as 3%, see tab. 2).
2. The effective maximum principal stress ($\sigma_{I\star}$) is greater than the critical stress σ_0 (taken as the yield stress, see tab. 2).
3. The nucleated porosity f_n is less than the volume fraction of particles which can cause void nucleation (f_N) (taken as the measured volume fraction of Fe rich particles).

The model has many parameters so that some of them are *a priori* fixed. The initial porosity f_0 corresponds to the volume fraction of coarse Mg_2Si particles that easily detach from the aluminum matrix[23]. q_1, q_2 and f_c are calibrated on unit cell calculations[31] carried out using the fit hardening law (eq. 1) as well as the measured f_0. The maximum nucleation porosity f_N is taken as the measured volume fraction of iron and silicon rich particles. The reference stress σ_0 is taken equal to the yield stress. Finally, the (A_n^s, N and A_n^0) parameters must be adjusted to represent crack initiation in smooth tensile and notched tensile samples. An attempt is done using the identified parameters in the work of Petit *et. al.*[23] who studied the same alloy. The cited authors determined the GTN parameters on compact tension specimens with high stress triaxiality levels (> 2.5). Those GTN parameters under estimated the porosity evolution when used to simulate the ductile behavior of NT samples in this study. This is of no surprise since the stress triaxiality level in the NT samples is lower than in the compact tensions samples. Consequently, the same GTN parameters (A_n^s, N and A_n^0) are reevaluated in this work to cover low and medium stress triaxiality levels (from 0.33 up to 2.0). The (f_c and f_R) parameters are also fit on the post–crack initiation phase of experiments in this work.

3.4.2 | Numerical results

Figure 8 displays simulations carried with the newly calibrated GTN parameters listed in tab. 2. More details concerning the finite element simulations and the used numerical methods are given in the appendix.The model provides good predictions of the damage behavior as the experimental and numerical crack–initiation and propagation phases are quite similar. Images from the tests are compared to the mesh images from the simulation to assure the similarity in both experimental and numerical post–necking phases. Elements of the numerical mesh are filled in black to be able to apply the ET method to the mesh images. Figure 9 compares the measured and simulated curvature radii based on sample and mesh images respectively. These encouraging results emphasize the advantage of the ET method in calibrating and validating the simulated post–crack initiation phase on such a low ductility alloy.

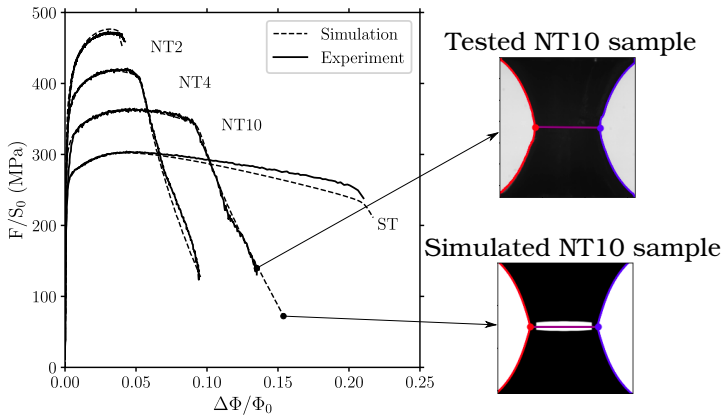

FIGURE 8 Simulated tensile tests with the new damage GTN model parameters calibrated on the post–necking phase in ST and NT experiments. The white space in the center of the simulated NT10 sample represents the crack.

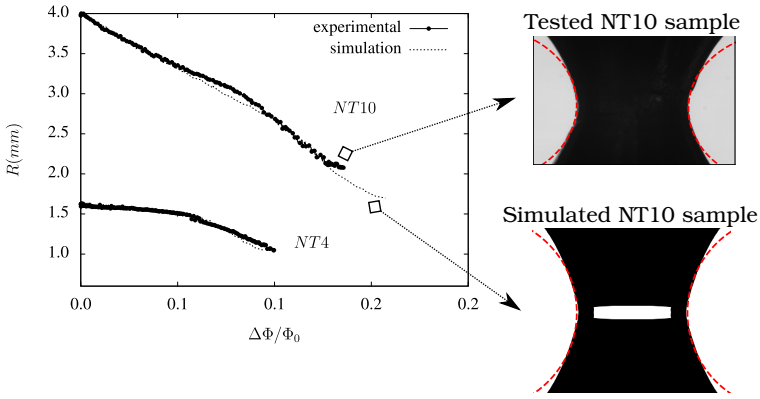

FIGURE 9 Notch curvature radius R calculated ($\eta = 1$) by applying the ET method on test and numerical mesh images. Bottom image displays a numerical mesh with a propagated crack while the top image is taken from a NT10 experimental test.

4 | CASE STUDY 2: ET METHOD APPLIED TO THE STUDY OF THE ANISOTROPIC ELASTIC–PLASTIC BEHAVIOR OF A X52 STEEL

4.1 | Material

Construction steels for pipelines are fabricated from hot rolled sheet metals. Large diameter pipes are then produced by UOE forming[1]. The material has an anisotropic plastic behavior due to crystallographic texture developed during the fabrication process[41]. Thus, it is important to keep track of the material principal axes (with respect to the metal forming process). The longitudinal direction corresponding to the rolling direction is hereby referred to as L; the transverse direction as T and the short transverse (thickness) direction as S. D stands for the diagonal direction (45° between direction L and T in the sheet plane).

In this study, the behavior of a "vintage" (produced in 1968) X52 API grade steel is investigated. Its chemical composition is shown in table 3. One can notice the high sulfur content which is 10 times higher than in modern steels.

TABLE 3 Studied X52 grade of steel chemical composition by %wt.

C	Mn	S	Al	Si	Cr	Cu	Mo	V	Ti	Fe
0.17	1.22	0.054	0.036	0.27	≤ 0.01	0.06	≤ 0.01	≤ 0.01	≤ 0.01	bal.

4.2 | Anisotropic plastic behavior

The plastic anisotropic behavior of the material is studied using smooth and notched tensile bars. The ET method is employed using two cameras (see fig. 2) which track the radial deformation in the chosen directions perpendicular to the loading direction. For example, deformation is tracked along T and S for a test loaded in the L direction. The same protocol as in the case of the AA6061-T6 tests is used. The specimens have a minimal diameter Φ_0 of 6 mm and a radius R_0 equal to 6, 2.4 and 1.2 mm (respectively corresponding to NT10, NT4 and NT2 specimens). The extensometer initial length (L_0) is 25 mm for NT specimens and 13.2 mm for ST specimens. As the study is only concerned with the elastic–plastic behavior, results are shown up to the onset of failure. It is assumed that ductile damage has a negligible effect on the overall behavior before the onset of failure. Tests are repeated twice or thrice. Only one test is shown for every given specimen/loading direction configuration.

Results of ST specimens tested along the L, T and D directions are shown in fig. 10(a, b). Fig. 10(a) shows the nominal stress (F/S_0) as a function of the nominal strain ($\Delta l/l_0$) up to the onset of necking. A Lüders plateau is observed in all cases up to a strain equal to 2%. A slight stress anisotropy is observed. Tab. 4 summarizes the tensile properties and number studied ST samples along different loading directions.

Fig. 10(b) shows the true strain along the direction orthogonal to both the loading direction and the S–direction ($\varepsilon_\perp = \log(\Phi_\perp/\Phi_0)$) as a function of the true strain along the S–direction ($\varepsilon_S = \log(\Phi_S/\Phi_0)$). $\Phi_\perp$ and Φ_S are respectively the diameters measured for the orthogonal and the S directions. The ET method allows measuring strain beyond the onset of necking which is indicated by dots. Results remarkably show that the initial strain ratio (Lankford's coefficient) $\mathcal{L} = \varepsilon_\perp/\varepsilon_S$ remains unchanged after the onset of necking. Lankford's coefficients for the three loading directions are 0.81, 0.74 and 1.01 for the T, L and D directions respectively. The lower maximum strain for testing along the T direction is due to the lower ductility of the material when tested in that direction. This behavior is often observed in line pipe steels[42;43]. The Lankford coefficient are lower than 1 for L and T loadings whereas it is close to 1 for D loading. These trends are commonly observed for UOE pipes[41;44]. In the

[1]UOE forming is a manufacturing process where the plate material is first deformed into an U-shape then an O-shape. The pipe seam is then welded. The pipe is finally expanded using an internal mandrel. To achieve low ovality, the pipe is typically expanded by 0.8–1.3% from its diameter after the O-step[40].

TABLE 4 Monotonic tensile properties and number of studied X52 steel ST samples in three loading directions: T, L and D

Loading direction	Tested samples	Yield strength (MPa)		Ultimate tensile strength (MPa)		Uniform elongation (%)	
		Avg.	*Std. dev. (%)*	*Avg.*	*Std. dev. (%)*	*Avg.*	*Std. dev. (%)*
T	5	408	5.0	551	3.6	17.4	1.0
L	4	410	8.2	553	7.4	15.3	0.5
D	2	410	0.5	559	1.5	16.5	0.5

present case, the Lankford coefficients are evaluated for the entire strain range. They are computed using the total strain as it impossible to experimentally separate elastic and plastic stains after necking.

Diameter variations for ST and NT specimens are shown in fig. 10(c, d) for both L and T loading directions. NT samples' results are consistent with the obtained results on smooth tensile bars. Three NT samples are tested for each geometry and every loading direction. Deformation tends to be maximum along the S direction for both loading directions. Stress anisotropy is negligible. One can also notice that strain to failure is smaller for T loading.

4.3 | Identification of a model for plastic anisotropy

Experimental results presented in the previous section are now used to adjust a model to represent the plastic anisotropy of the material. In ST specimens, the ET technique can be used beyond the necking point so that work hardening can be adjusted with a good accuracy over a large plastic strain range which guarantees that no extrapolation is used to simulate the behavior of the entire database. As the material exhibits a very low stress anisotropy but a pronounced plastic flow anisotropy, a Hill type model[45] cannot be used in the present case. This is because the normality rule links stress and strain anisotropies. Given the reduced number of material parameters, both phenomena cannot be simultaneously adjusted. The same also holds for the non–quadratic law proposed by Barlat *et. al.*[46]. The model proposed to describe the anisotropic plastic behavior of the material circumvents this limitation and is briefly presented below.

The BB04 model used in this study to describe plastic anisotropy is initially developed in the case of aluminum alloys[47;48] but is also applied to line pipe steels[41;44;42]. It is a generalization of previously published models[49;46]. An anisotropic scalar stress measure, σ_E, is defined as a weighted average of N anisotropic scalar stress measures σ_{Ei}:

$$\sigma_E = \left(\sum_{k=1}^{N} \alpha_k \sigma_{Ek}^a \right)^{1/a} \tag{10}$$

where α_k are weight factors such that $\sum_k \alpha_k = 1$. In the following, two anisotropic scalar stress measures ($N = 2$) are used to define σ_E as in[47;41]. One first defines two modified stress deviators:

$$\boldsymbol{s}_k = \mathbb{L}_k : \boldsymbol{\sigma} \qquad k = 1, 2 \tag{11}$$

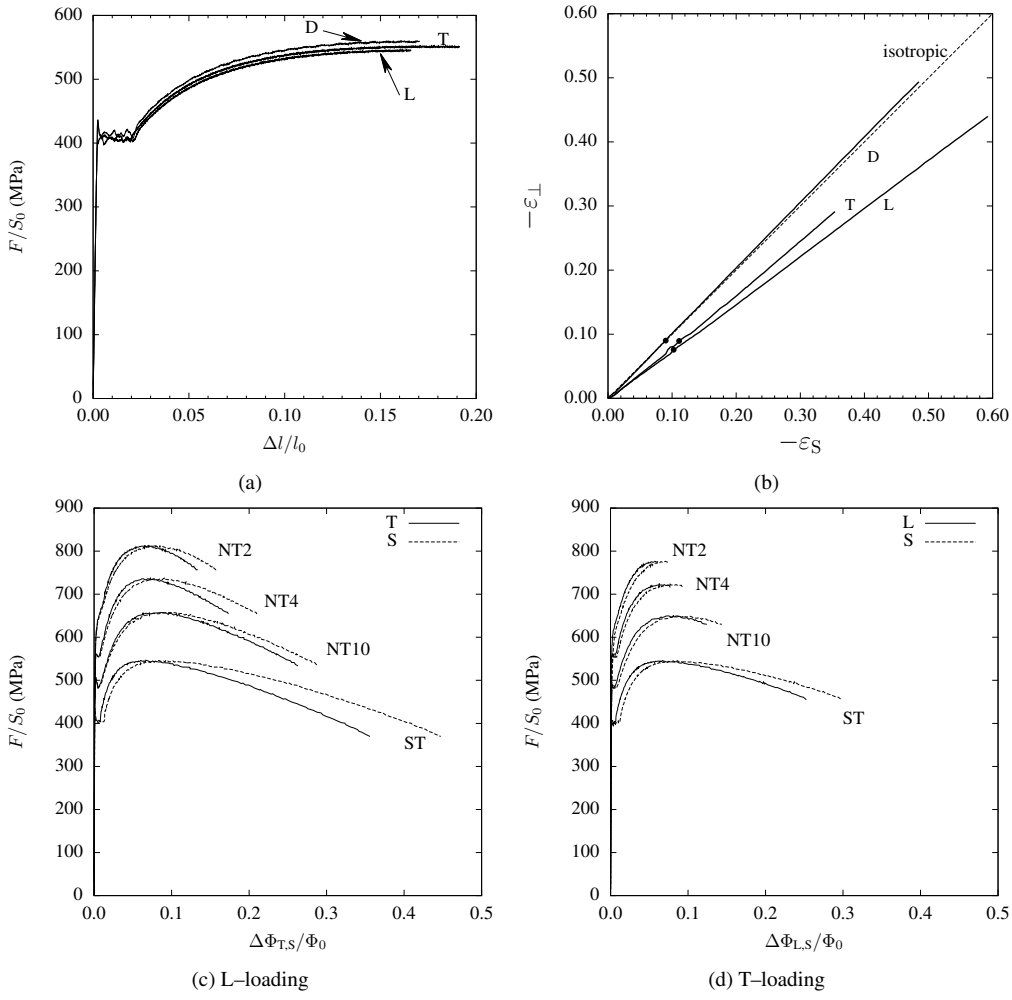

FIGURE 10 Tensile tests performed on the X52 vintage steel. (a) Nominal stress—strain curves along L, T, and D directions, (b) Deformation ($-\Delta\Phi_\perp/\Phi_0$) along the direction orthogonal to both the loading direction and the S–direction as a function of the deformation along the S–direction ($-\Delta\Phi_S/\Phi_0$). Dots indicate the onset of necking. Normalized force — diameter variation curves for (c) L—loading and (d) T—loading.

$\mathbf{a = b_1 = b_2}$			α_1	α_2	
13.8			0.64	0.36	
$\mathbf{c^1_{TT}}$	$\mathbf{c^1_{LL}}$	$\mathbf{c^1_{SS}}$	$\mathbf{c^1_{TL}}$	$\mathbf{c^1_{LS}}$	$\mathbf{c^1_{ST}}$
0.82	1.00	0.91	0.98	1.50	1.15
$\mathbf{c^2_{TT}}$	$\mathbf{c^2_{LL}}$	$\mathbf{c^2_{SS}}$	$\mathbf{c^2_{TL}}$	$\mathbf{c^2_{LS}}$	$\mathbf{c^2_{ST}}$
1.18	1.17	0.94	0.94	1.33	0.77

σ_L	σ_0	Q_1	b_1	Q_2	b_2	H
400 (MPa)	368 (MPa)	292 (MPa)	7.4	82 (MPa)	28	63 (MPa)

TABLE 5 Model parameters used to define the anisotropic scalar stress measure (σ_E) and the flow stress ($R(p)$)

where the fourth order tensors $\mathbb{L}_k$ are expressed using Voigt notations as follows:

$$\mathbb{L}_k = \begin{pmatrix} \frac{1}{3}(c^k_{LL} + c^k_{SS}) & -\frac{1}{3}c^k_{SS} & -\frac{1}{3}c^k_{LL} & 0 & 0 & 0 \\ -\frac{1}{3}c^k_{SS} & \frac{1}{3}(c^k_{SS} + c^k_{TT}) & -\frac{1}{3}c^k_{TT} & 0 & 0 & 0 \\ -\frac{1}{3}c^k_{LL} & -\frac{1}{3}c^k_{TT} & \frac{1}{3}(c^k_{TT} + c^k_{LL}) & 0 & 0 & 0 \\ 0 & 0 & 0 & c^k_{TL} & 0 & 0 \\ 0 & 0 & 0 & 0 & c^k_{LS} & 0 \\ 0 & 0 & 0 & 0 & 0 & c^k_{ST} \end{pmatrix} \tag{12}$$

$c^k_{LL} \dots c^k_{ST}$ are coefficients introduced to represent anisotropy. Using the eigenvalues of $\boldsymbol{s}_k$ ($s^1_k \geq s^2_k \geq s^3_k$), the stress measures σ_{Ek} are defined as:

$$\sigma_{E1} = \left(\frac{1}{2} \left(|s^2_1 - s^3_1|^{b_1} + |s^3_1 - s^1_1|^{b_1} + |s^1_1 - s^2_1|^{b_1} \right) \right)^{1/b_1} \tag{13}$$

$$\sigma_{E2} = \left(\frac{3^{b_2}}{2^{b_2} + 2} \left(|s^1_2|^{b_2} + |s^2_2|^{b_2} + |s^3_2|^{b_2} \right) \right)^{1/b_2} \tag{14}$$

The exponents a, b_1 and b_2 are used to modify the shape of the yield surface. In the following, one will assume $a = b_1 = b_2$. The yield surface is then expressed while assuming pure isotropic hardening as follows:

$$S = \sigma_E - \sigma_F(p) \tag{15}$$

where $\sigma_F(p)$ is a function of the accumulated plastic strain (p) representing the flow stress. The plastic strain rate tensor, $\dot{\boldsymbol{\varepsilon}}_p$, is obtained assuming the normality rule so that: $\dot{\boldsymbol{\varepsilon}}_p = \dot{p}\partial S/\partial\boldsymbol{\sigma}$. p is such that: $\dot{\boldsymbol{\varepsilon}}_p : \boldsymbol{\sigma} = \dot{p}\sigma_E$.

The various parameters of the model are adjusted using the guidelines proposed in[47]. Fitted values are gathered in tab. 5. The flow stress is defined as:

$$\sigma_F(p) = \max\left(\sigma_L, \sigma_0 + Q_1(1 - \exp(-b_1 p)) + Q_2(1 - \exp(-b_2 p)) + Hp\right) \tag{16}$$

where σ_L represents the Lüders stress which is fixed to 400 MPa. The hardening function combines a linear and two non linear terms in order to be able to represent hardening over a large strain range ($p \in [0 : 1.2]$). The Young's modulus is equal to 210 GPa and the Poisson's ratio is 0.3. The simulated length of the Lüders plateau is about 1%.

The predictions of the model are compared with experiments in fig. 11. More details concerning the numerical methods

are given in the appendix. The latter elaborates the fact that the model is able to represent the quasi–isotropic stress behavior (fig. 11(a)) while, at the same time, it also well represents the anisotropic strain behavior (fig. 11(b)).

Comparisons between experimental and simulated results are also shown in fig. 11(c, d) for both L (fig. 11(c)) and T (fig. 11(d)) loading directions. A good agreement is found between experimental and simulated results.

To illustrate the benefit of the developed model for plastic anisotropy, simulations using von Mises plasticity are also plotted in fig. 11(c, d) (red dashed lines). The hardening function is fitted using the F/S_0—$\Delta\Phi/\Delta\Phi_S$ curves for tests carried along the D direction as the strain behavior is almost isotropic in this case. Fitting the behavior for T or L loading can also be performed using the geometric mean of the diameters along the S and $\perp$ directions in order to keep the same cross section. One must note that fitting the model for strains less than the necking strain (≈ 0.17) leads to a very poor representation of F/S_0—$\Delta\Phi/\Phi_0$ curves as the fitted hardening is used far beyond its identification domain (extrapolation).

Comparisons between experiments and simulations using the BB04 model show a relatively good agreement for tensile tests. As notch severity is increased, the predicted maximum load overestimates the maximum load which is well represented by the BB04 model. This observation is also noted in[47]. This corresponds to a non quadratic yield surface width $a > 4$.

5 | CONCLUSIONS AND REMARKS

The ET technique was developed in other studies to investigate large strains as well as the elastic–plastic behavior well beyond the necking strain. The aim of this work is to extend the ET method to two challenging case studies: the post–necking behavior and failure in a low ductility AA6061-T6 and the plastic anisotropic behavior of line pipe steels. The mentioned case studies cannot be carried out using the conventional extensometer-based measuring techniques.

In the first case study, it is necessary to carry the failure assessment on various stress triaxiality levels. This is achieved via a campaign of tensile testing on round notched samples with different curvature radii (*i.e.* different stress triaxiality levels). The principal conclusions made on the obtained results from the first case study are highlighted below:

- The AA6061-T6 usually incurs rapid failure after the maximum load is reached during the tensile test. However, the post–necking phase is captured in this work thanks to the "deformation controlled" technique. The latter helped in maintaining a relatively stable crack propagation phase. This technique is proved to be essential for calibrating the GTN damage parameters on tensile experimental data.
- The GTN damage parameters are first taken from other work that studied the same alloy under high stress triaxiality levels (> 2.5 in CT samples). The initial model parameters overestimated the deformation at failure in the simulated ST and NT sample. However, the post–necking data obtained by the ET method help reevaluate the damage parameters. The latter fit low (0.33 in ST samples) and medium (0.6-2.0 in NT samples) stress triaxiality levels. As a result, the simulated stress—radial deformation curves are in good agreement with the experiments.

The ET method is secondly employed to study the continuous evolution of the anisotropic behavior of line pipe steels to better understand the macroscopic behavior of the studied steel. The main conclusions made on the obtained results from the second case study are highlighted below:

- The ET method allows continuously observing the anisotropical behavior of line pipe steels during the entire tensile test. The "old-fashioned" alternative is to rely on the post–mortem study of the fracture surfaces to analyze the anisotropy. However,

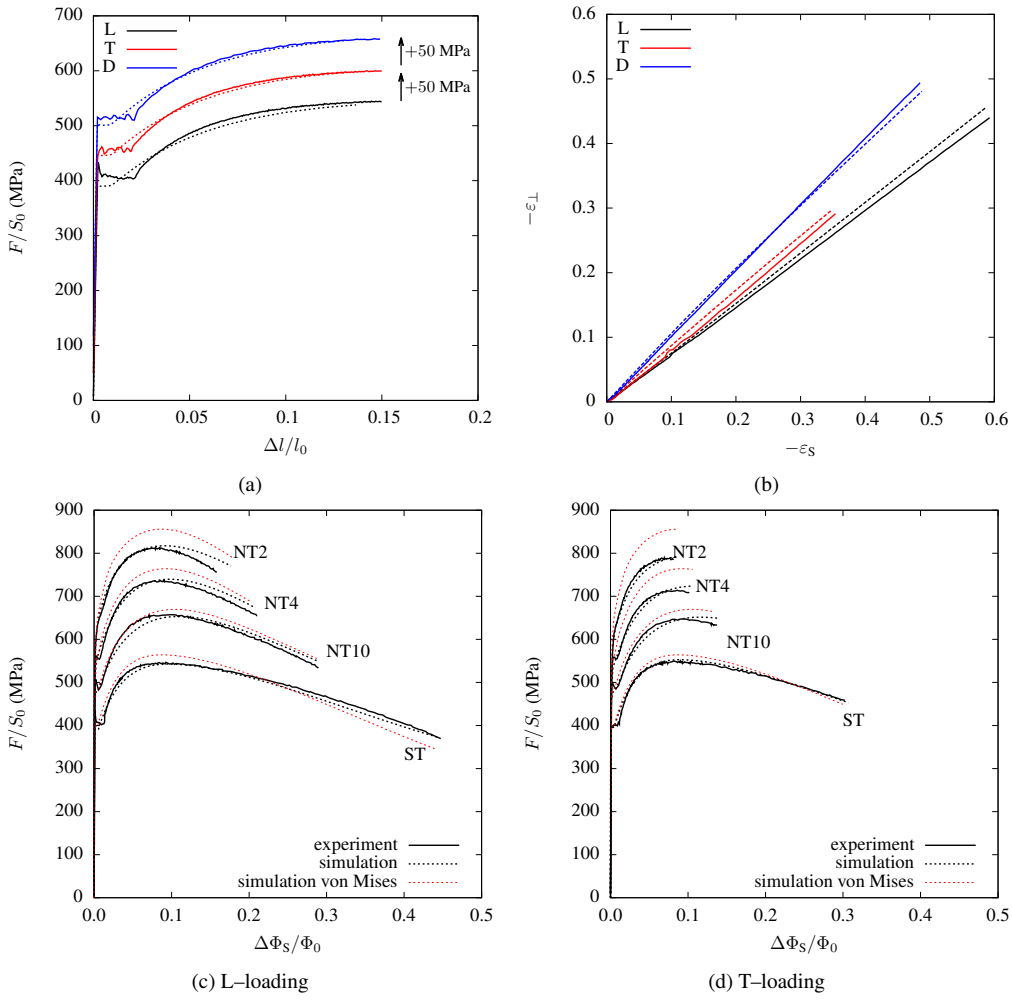

FIGURE 11 Comparison between experimental and simulated (a) nominal stress — elongation ($\Delta l/l_0$), a shift of 50MPa is applied to differentiate between L, T and D directions, (b) $\Delta\Phi_\perp/\Phi_0$ — $\Delta\Phi_S/\Phi_0$ curves, nominal stress — diameter variation along S curves for (c) L—loading and (d) T—loading (X52 steel) (Full lines: experiment, dashed lines: simulation, red dashed lines (c, d): simulation obtained assuming von Mises plasticity).

in this study, the evolution of Lankford factor is continuously estimated for both tested directions during the tests conducted on ST specimens.

- The collected experimental data via the ET method give significant amount of information regarding the true radial strain in different loading directions. As a result, the parameters of the BB anisotropic plastic constitutive law are identified accurately.

ACKNOWLEDGMENTS

Authors of this work would like to thank the *Laboratoire de comportement des matériaux irradiés (LCMI)* laboratory at CEA Saclay for providing the aluminum alloy used in this study. They would like to thank as well the *RICE* research center of GRTgaz France for supplying the X52 alloy studied in this work. Special thanks to the machining and mechanical testing teams at *Centre des matériaux* for their extraordinary work.

CONFLICT OF INTEREST

The authors declare that they have no known competing financial interests or personal relationships that could have appeared to influence the work reported in this paper.

REFERENCES

1. Zhang Z, Hauge M, Ødegård J, Thaulow C. Determining material true stress–strain curve from tensile specimens with rectangular cross–section. *Int. J. Solids Structures* 1999; 36: 3497–3516.

2. Tu S, Ren X, He J, Zhang Z. Experimental measurement of temperature-dependent equivalent stress-strain curves of a 420 MPa structural steel with axisymmetric notched tensile specimens. *Eng. Fail. Anal.* 2019; 100: 312–321

3. Bridgman PW. Effects of High Hydrostatic Pressure on the Plastic Properties of Metals. *Rev. Mod. Phys.* 1945; 17: 3–14

4. Bao Y, Wierzbicki T. On fracture locus in the equivalent strain and stress triaxiality space. *Int. J. Mech. Sci.* 2004; 46(1): 81-98.

5. Tu S, Ren X, He J, Zhang Z. A method for determining material's equivalent stress-strain curve with any axisymmetric notched tensile specimens without Bridgman correction. *Int. J. Mech. Sci.* 2018; 135: 656-667

6. Versaillot P, Zhao Z, Wu Y. A new theoretical method for predicting the elastoplastic behavior of ductile metallic materials. *Int. J. Mech. Sci.* 2021; 200: 106450

7. Bao Y, Wierzbicki T. On the cut-off value of negative triaxiality for fracture. *Eng. Fract. Mech.* 2005; 72: 1049-1069.

8. Bai Y, Teng X, Wierzbicki T. On the Application of Stress Triaxiality Formula for Plane Strain Fracture Testing. *J. Engng Mater. Technol.* 2009; 131(2)

9. Mirone G. A new model for the elastoplastic characterization and the stress–strain determination on the necking section of a tensile specimen. *Int. J. Solids Structures* 2004; 41: 3545–3564.

10. Zhang Z, Haugeb M, Thaulow C, Ødegård J. A notched cross weld tensile testing method for determiningtrue stressstrain curves for weldments. *Eng. Fract. Mech.* 2001; 69: 353–366

11. Olden V, Zhang Z, Østby E, Nyhus B, Thaulow C. Notch tensile testing of high strength steel weldments. In: ; 2002

12. Hopperstad O, Børvik T, Langseth M, Labibes K, Albertini C. On the influence of stress triaxiality and strain rate on the behaviour of a structural steel. Part I. Experiments. *Eur. J. Mech./A* 2003; 22(1): 1-13

13. Vilamosa V, Clausen AH, Fagerholt E, Hopperstad OS, Borvik T. Local Measurement of Stress–Strain Behaviour of Ductile Materials at Elevated Temperatures in a Split-Hopkinson Tension Bar System. *Strain* 2014; 50(3): 223–235

14. Tu S, Ren X, Kristensen T, He J, Zhang Z. Study of low-temperature effect on the fracture locus of a 420-MPa structural steel with the edge tracing method. *Fatigue and Fract. Engng Mater. Struct.* 2018; 41: 1649 1661

15. Mirone G, Barbagallo R. How sensitivity of metals to strain, strain rate and temperature affects necking onset and hardening in dynamic tests. *Int. J. Mech. Sci.* 2021; 195: 106249

16. Ghahremaninezhad A, Ravi-Chandar K. Ductile failure behavior of polycrystalline Al 6061-T6. *Int. J. Frac.* 2012; 174(2): 177-202.

17. Hancock J, Mackenzie A. Mechanisms of ductile failure in high-strength steels subjected to multi- axial stress states. *J. Mech. Phys. Solids* 1976; 24: 147-160.

18. Petit T, Ritter C, Besson J, Morgeneyer T. Impact of machine stiffness on "pop-in" crack propagation instabilities. *Eng. Fract. Mech.* 2018; 202: 405–422.

19. Buades A, Coll B, Morel J. Non-Local Means Denoising. *IPOL J. Image Processing Online* 2011: 208 - 212

20. Xu X, Xu S, Jin L, Song E. Characteristic analysis of Otsu threshold and its applications. *Pattern Recognition Letters* 2011; 32(7): 956-961

21. Hasting H, Lefebvre W, Marioara C, et al. Comparative study of the β" phase in a 6xxx Al alloy by 3DAP and HRTEM. *Surf. Interface Anal.* 2007; 39(7): 189–194

22. Shen Y, Morgeneyer T, Garnier J, Allais L, Helfen L, Crépin J. Three-dimensional quantitative in situ study of crack initiation and propagation in AA6061 aluminum alloy sheets via synchrotron laminography and finite-element simulations. *Acta Mater.* 2013; 61: 2571–2582

23. Petit T, Besson J, Ritter C, Colas K, Helfen L, Morgeneyer T. Effect of hardening on toughness captured by stress-based damage nucleation in 6061 aluminum alloy. *Acta Mater.* 2019; 180: 349-365

24. Mohr D, Marcadet S. Micromechanically-motivated phenomenological Hosford-Coulomb model for predicting ductile fracture initiation at low stress triaxialities. *Int. J. Solids Structures* 2015; 67-68: 40-55.

25. Defaisse C, Mazière M, Marcin L, Besson J. Ductile fracture of an ultra-high strength steel under low to moderate stress triaxiality. *Eng. Fract. Mech.* 2018; 194: 301–318.

26. Farahani B, Amaral R, Belinha J, Tavares P, Moreira P. A GTN Failure Analysis of an AA6061-T6 Bi-Failure Specimen. *Procedia Structural Integrity* 2017; 5: 981-988

27. Dorbane A, Ayoub G, Mansoor B, Hamade R, Kridli G, Imad A. Observations of the mechanical response and evolution of damage of AA 6061-T6 under different strain rates and temperatures. *Mater. Sci. Engng A* 2015; 624: 239-249

28. Chu C, Needleman A. Void nucleation effects in biaxially stretched sheets. *J. Engng Mater. Technol.* 1980; 102: 249–256.

29. Tvergaard V. Influence of voids on shear band instabilities under plane strain condition. *Int. J. Frac.* 1981; 17(4): 389–407.

30. Tvergaard V. On the localization in ductile materials containing spherical voids. *Int. J. Frac.* 1982; 18(4): 237–252.

31. Faleskog J, Gao X, Shih C. Cell model for nonlinear fracture analysis — I. Micromechanics calibration. *Int. J. Frac.* 1998; 89: 355–373.

32. Gao X, Faleskog J, Shih C. Cell model for nonlinear fracture analysis — II. Fracture–process calibration and verification. *Int. J. Frac.* 1998; 89: 375–398.

33. Xia L, Shih CF. Ductile crack growth — I. A numerical study using computational cells with microstructurally-based length scales. *J. Mech. Phys. Solids* 1995; 43: 233–259.

391 34. Xia L, Shih CF. Ductile crack growth — II. Void nucleation and geometry effects on macroscopic fracture behaviour. *J. Mech. Phys. Solids* 1995; 43: 1953–1981.

393 35. Pardoen T, Hutchinson J. An extended model for void growth and coalescence. *J. Mech. Phys. Solids* 2000; 48(12): 2467-2512.

394 36. Tvergaard V, Needleman A. Analysis of the cup–cone fracture in a round tensile bar. *Acta Metall.* 1984; 32: 157–169.

395 37. Besson J, Steglich D, Brocks W. Modeling of crack growth in round bars and plane strain specimens. *Int. J. Solids Structures* 2001; 38(46–47): 8259–8284.

397 38. Zhang Z, Thaulow C, Ødegård J. A complete Gurson model approach for ductile fracture. *Eng. Fract. Mech.* 2000; 67(2): 155–168.

398 39. Dalloz A, Besson J, Gourgues-Lorenzon AF, Sturel T, Pineau A. Effect of shear cutting on ductility of a dual phase steel. *Eng. Fract. Mech.* 2009; 76(10): 1411-1424.

400 40. Herynk MD, Kyriakides S, Onoufriou A, Yun HD. Effects of the UOE/UOC pipe manufacturing processes on pipe collapse pressure. *Int. J. Mech. Sci.* 2007; 49(5): 533-553.

402 41. Tanguy B, Luu T, Perrin G, Pineau A, Besson J. Plastic and damage behavior of a high strength X100 pipeline steel: experiments and modelling. *Int. J. of Pressure Vessels and Piping* 2008; 85(5): 322-335.

404 42. Shinohara Y, Madi Y, Besson J. Anisotropic ductile failure of a high-strength line pipe steel. *Int. J. Frac.* 2016; 197: 127-145.

405 43. Madi Y, Garcia JM, Proudhon H, et al. On the origin of the anisotropic damage of X100 line pipe steel. Part I: In-situ synchrotron tomography experiments. *Integrating Material and Manufacturing Innovations* 2019.

407 44. Shinohara Y, Madi Y, Besson J. A combined phenomenological model for the representation of anisotropic hardening behavior in high strength steel line pipes. *Eur. J. Mech./A* 2010; 29(6): 917–927.

409 45. Hill R. *The mathematical theory of plasticity*. Clarendon Press, Oxford . 1950.

410 46. Barlat F, Lege D, Brem J. A six–component yield function for anisotropic materials. *Int. J. Plasticity* 1991; 7: 693–712.

411 47. Bron F, Besson J. A yield function for anisotropic materials. Application to aluminium alloys. *Int. J. Plasticity* 2004; 20: 937-963.

412 48. Zhang S, Leotoing L, Guines D, Thuillier S, Zang S. Calibration of anisotropic yield criterion with conventional tests or biaxial test. *Int. J. Mech. Sci.* 2014; 85: 142-151.

414 49. Karafillis A, Boyce M. A general anisotropic yield criterion using bounds and a transformation weighting tensor. *J. Mech. Phys. Solids* 1993; 41: 1859–1886.

416 50. Besson J, Foerch R. Large scale object–oriented finite element code design. *Comp. Meth. Appl. Mech. Engng* 1997; 142: 165–187.

417 51. Sidoroff F, Dogui A. Some issues about anisotropic elastic-plastic models at finite strain. *Int. J. Solids Structures* 2001; 38: 9569-9578.

419 52. Feld-Payet S, Feyel F, Besson J. Finite element analysis of damage in ductile structures using a nonlocal model combined with a three-field formulation. *Int. J. Damage Mech.* 2011; 20: 655-680.

421 53. Mediavilla J, Peerlings R, Geers M. Discrete crack modelling of ductile fracture driven by non-local softening plasticity. *Int. J. Numer. Meth. Engng* 2006; 66(4): 661-688.

423 54. Liu Y, Murakami S, Kanagawa Y. Mesh–dependence and stress singularity in finite element analysis of creep crack growth by continuum damage mechanics approach. *Eur. J. Mech./A* 1994; 13A(3): 395–417.

425 55. Rousselier G. Ductile fracture models and their potential in local approach of fracture. *Nucl. Eng. Des.* 1987; 105: 97–111.

426 56. Siegmund T, Brocks W. A numerical study on the correlation between the work of separation and the dissipation rate in ductile fracture. *Eng. Fract. Mech.* 2000; 67: 139-154.

A | NUMERICAL METHODS

Finite element (FE) simulations are carried out in this study via the Zset general purpose object oriented finite element software [50]. Ductile failure in aluminum alloys or plastic anistoropy in line pipe steels are two mechanical engineering problems that require a finite–strain formalism when implementing the constitutive equations. This is done by a generic formulation based on a reference frame which assures maintaining the standard small strain formulation while using an additive strain rate decomposition (*i.e.* $\dot{\varepsilon} = \dot{\varepsilon}_e + \dot{\varepsilon}_p$ where $\dot{\varepsilon}$ is the strain rate tensor and $\dot{\varepsilon}_e$ the elastic strain rate tensor) [51].

A.1 | FE simulations in case study 1: Plasticity and failure of a 6061-T6 aluminum alloy

For FE simulations carried out in the first case study, 2D meshes of the axisymmetric ST and NT samples are obtained with 8-node quadrangle elements containing 4 integration points (reduced integration). Symmetry conditions are used so that only $^1/_4$ of the ST and NT samples are meshed. The mesh size (h in tab. 2) is taken as 100×100 μm^2 which is based on the average estimated distance between large constituent particles in the AA6061-T6 studied alloy.

The used GTN damage models leads to material softening which results in strain and damage localization within one row of elements. As a result, the simulation results strongly depend on the mesh size. To overcome this issue, models integrating material internal lengths can be used (*e.g.* [52;53]). However, these models are still in an early development phase. The pragmatic solution chosen in this study is to fix a mesh size along the crack path [54;55] (minimal cross-section diamater in tensile samples). The fixed mesh size controls the fracture energy in the case of mesh dependent simulations [56].

The material integration point is considered as broken when f_* reaches $1/q_1 - \epsilon$ (with $\epsilon = 10^{-3}$). Then, its behavior is replaced by an elastic behavior with a very low stiffness (Young modulus: $E = 1$ MPa). When 2 out of 4 integration points are considered as broken in the 2D element, the latter is removed from the mesh. Displacement increments at nodes belonging to removed elements are then fixed to avoid a singular global stiffness matrix.

A.2 | FE simulation in case study 2: ET method applied to the study of the anisotropic elastic–plastic behavior of a X52 steel

Elastic–plastic FE simulations carried out in the second case study are mainly used to optimize parameters of the hardening law (see eq. 16 and tab. 5). Unlike the first case study, the line pipe steels have a significant anistropic plastic behavior. Therefore, 3D meshes are necessary. A 20-node 3D hexahedral element with 8 integration points (reduced integration) is used to mesh the ST and NT samples. The mesh size is taken as $100 \times 100 \times 100$ μm^3.